https://science.org/doi/10.1126/science.abj3210

Title: Grain boundary velocity and curvature are not correlated in Ni polycrystals

Authors: Aditi Bhattacharya[1], Yu-Feng Shen[2]†, Christopher M. Hefferan[2]‡, Shiu Fai Li[2]§, Jonathan Lind[2]¶, Robert M. Suter[2], Carl E. Krill III[3], Gregory S. Rohrer[1]*

Affiliations:

[1]Department of Materials Science and Engineering, Carnegie Mellon University; Pittsburgh, Pennsylvania 15213, USA.

[2]Department of Physics, Carnegie Mellon University; Pittsburgh, Pennsylvania 15213, USA.

[3]Institute of Functional Nanosystems, Ulm University; 89081 Ulm, Germany.

*Corresponding author. Email: gr20@andrew.cmu.edu

†Present address: Morgan Stanley & Co LLC

‡Present address: RJ Lee Group; Monroeville, PA 15146, USA.

§Present address: Blue River Technology; Sunnyvale, CA 94086, USA.

¶Present address: Materials Engineering Division, Lawrence Livermore National Laboratory; Livermore, CA 94550, USA.

Published Oct. 8 2021, https://science.org/doi/10.1126/science.abj3210

Abstract: Grain boundary velocity has been believed to be correlated to curvature, and this is an important relationship for modeling how polycrystalline materials coarsen during annealing. We determined the velocities and curvatures of approximately 52,000 grain boundaries in a Ni polycrystal using three-dimensional orientation maps measured by high-energy diffraction microscopy before and after annealing at 800 °C. Surprisingly, the grain boundary velocities and curvatures are uncorrelated. Instead, we found strong correlations between the boundary velocity and the five macroscopic parameters that specify grain boundary crystallography. The sensitivity of the velocity to grain boundary crystallography might be the result of defect-mediated grain boundary migration or the anisotropy of the grain boundary energy. The absence of a correlation between velocity and curvature likely results from the constraints imposed by the grain boundary network and implies the need for a new model for grain boundary migration.

One-Sentence Summary: Measured grain boundary velocities and curvatures in a polycrystal are uncorrelated, contradicting the accepted theory.

Main Text: During the high-temperature processing of polycrystalline materials, grain boundary migration is responsible for creating the final microstructure and therefore influences many of a material's macroscopic properties. This process occurs in a wide range of technologically important materials. For example, the internal configuration of grain boundaries influences the strength and electronic conductivity of polycrystalline Cu within integrated circuits (*1*) and the toughness of high-strength automotive steels (*2*). The arrangement of grain boundaries also has a profound effect on the performance of functional materials used in, for example, dielectric (*3*), thermoelectric (*4*), and photovoltaic devices (*5*). In the field of geology, models for grain boundary migration are important for understanding the properties of rocks in the Earth's mantle (*6*), and to extract knowledge about the paleoclimate from measurements of the microstructure of large ice sheets (*7*).

In cases where the energy stored in intragranular defects is minimal and boundary curvature is the most substantial driving force for grain growth, it is assumed that a grain boundary migrates toward its center of curvature at a velocity (v) that is directly proportional to the product of the grain boundary mean curvature (κ) and the grain boundary energy (γ), such that

$$v = M\kappa\gamma, \quad (1)$$

where M is a constant of proportionality referred to as the mobility (*8*). The linear relationship between grain boundary velocity and curvature has been verified by measurements (*9*) and simulations (*10*) of grain boundary migration in bicrystals. The simple linear relation also describes the average behavior of polycrystals if one accepts the average grain growth rate as a proxy for grain boundary velocity and the inverse mean grain size as a proxy for curvature (*11*). While the simple expression in Eq. 1 has been widely used to interpret simulations and experiments for nearly 70 years, mainly based on its validation in bicrystal studies, there is a range of evidence that neither the mobility nor the driving force ($\kappa\gamma$) are constants; instead, both are sensitive to the boundary structure. For example, Gottstein et al. (*9*) showed experimentally, and Olmsted et al. (*12*) showed using atomistic simulations, that M depends on boundary crystallography. In addition, Frolov (*13*) showed that M can vary with grain boundary complexion (structure), even when the macroscopic grain boundary degrees of freedom are constant. Similarly, γ varies with the grain boundary crystallography (*14*) and, because of this, the driving force is more complex. The actual driving force is proportional to the grain boundary stiffness, which is the sum of the boundary energy and the second derivative of that energy with respect to orientation in the directions of the principal curvatures (*15, 16*).

Despite its widespread acceptance, it remains an open question as to whether or not grain boundaries in polycrystals migrate at rates proportional to their curvatures. Boundaries in polycrystals differ from those in a bicrystal in an important way. Instead of being able to move freely, they are connected (on average) through five triple lines to ten other grain boundaries (*17*). Therefore, a grain boundary is unable to reduce its area without concomitant changes in the positions and areas of the connected boundaries, but these changes will not necessarily reduce the total energy. These mutual dependencies might explain how a critical population of slow-moving boundaries is able to bring about grain growth stagnation in the presence of curvature driving forces (*18*) or why boundary mobility measurements based on the assumed validity of Eq. 1 have led to inconsistent results for crystallographically identical boundaries (*19*).

The technical reason that grain boundary velocities have yet to be measured within polycrystalline materials is because there was no way until recently to measure the time dependence of the shapes and volumes of crystals embedded in an opaque material. The development of near-field high-energy diffraction microscopy (HEDM) during the past decade has made this possible (*20*). HEDM and related techniques have been used to study changes that occur during the annealing of polycrystals, including twin formation (*21*), coarsening (*22*), and grain growth (*19, 23-25*). We introduce a simple method to determine grain boundary velocities by measuring the microstructure at different time intervals. Using the three-dimensional microstructure of Ni imaged at six times during annealing at 800 °C, we measured the grain boundary curvatures and velocities of more than 5×10^4 grain faces of known crystallography (*26*). From these data, we assessed the validity of Eq. 1 for boundaries in polycrystals and determine how the velocities of grain boundaries depend on their crystallographic characteristics. The absence of a correlation between velocity and curvature has implications for modeling microstructure evolution.

The Ni specimen was annealed at 950 °C for 6 h prior to the grain growth experiment at 800 °C to achieve a minimal and constant dislocation density that would not affect the driving force for grain growth in a measurable way (*26*). We measured the grain boundary velocity using a method that we explain with reference to Fig. 1 (and show schematically in Fig. S1). The boundary in Fig. 1 is changing not only its position but also its shape and area, which made it impossible to track unit areas with different orientations. As a result, we determined the velocities from the volume exchanged between the grains, a method that provides an average velocity for the entire boundary and ameliorates the problems caused by the changing boundary shape (*26*). Each grain in the microstructure is assigned an identification (ID) number. For the boundary between the grain with ID = n and ID = m, any voxel that was part of grain n (m) in the first time step, and changed to grain m (n) in the second was counted. This count

provides a measure of the volume exchanged from *n* to *m* ($V_{n\to m}$) and from *m* to *n* ($V_{m\to n}$) in a certain time period. When volume is divided by the average area of the boundary between *n* and *m* in the two time steps ($\overline{A}_{n|m}$), and the time interval (Δt), the result has the dimensions of velocity (v):

$$v = \left|\frac{V_{n\to m}+V_{m\to n}}{\overline{A}_{n|m}\times\Delta t}\right|. \quad (2)$$

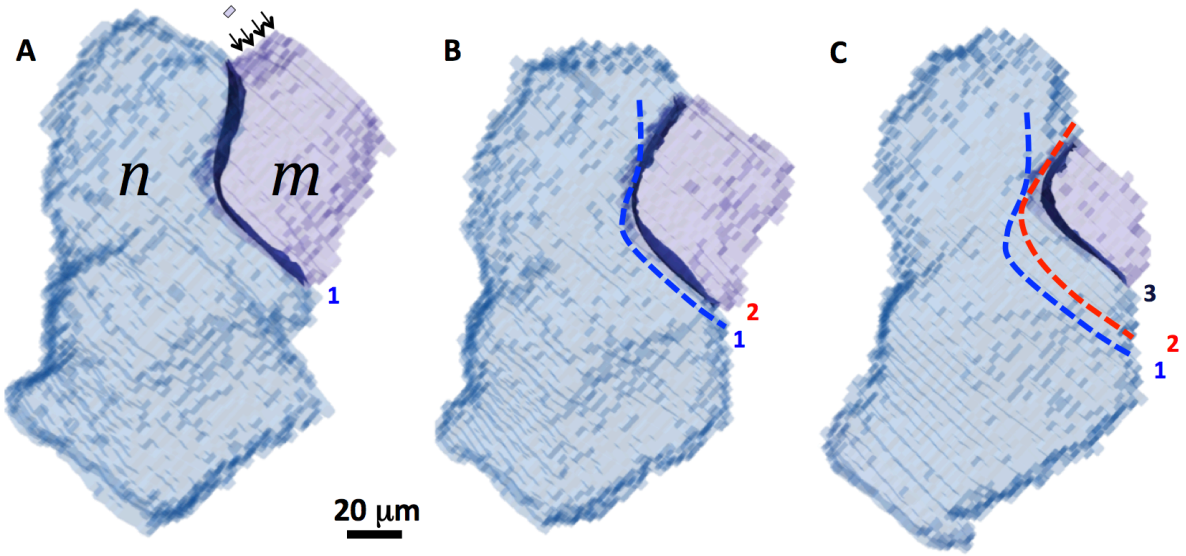

Fig. 1. Grain boundary migration. Two grains (*n* and *m*), showing individual voxels, at three different time steps. The boundary separating the grains is denoted by the dark blue shading. As the boundary between the two grains moves, some voxels that belong to grain *m* in (**A**) become part of grain *n* in (**B**) and (**C**). The four arrows at the top of A indicate four layers of voxels, and the small rectangle shows the projected area of a single 2.3 × 2.3 × 4.0 μm voxel. The interface position in A (labeled 1) is superposed on B and C. The interface position in B (labeled 2) is superposed on C.

The values used in Eq. 2 for the case illustrated by Fig. 1 can be found in Table S1. Like all grain boundary properties, v is unsigned, because it must obey grain exchange symmetry (*26*). Once completed, our analysis encompassed 51,794 grain faces. The distribution of velocities (Fig. S1A) had a mean of 0.1 μm/min and a standard deviation of the same order. The distribution of curvatures (Fig. S1B) had a mean of 0.05 μm^{-1}, and the standard deviation was 0.08 μm^{-1}. The magnitude of the mean corresponds to grains having a mean radius of 20 μm, consistent with the average grain size in this microstructure. All boundaries are represented by a set of triangular mesh elements, and, for each element, we determined the orientation, area, curvature, and velocity.

We illustrate the relationship between the grain face-averaged grain boundary velocity and curvature with scatter plots (Fig. 2A-B). When the data are viewed throughout the entire domain (Fig. 2A), the majority falls near

the origin, with no apparent correlation between the quantities. A closer look at the domain near the origin, containing 84 % of the data, confirms the lack of correlation (Fig. 2B). To examine average velocities of boundaries with similar curvature, we binned the boundaries into curvature intervals of 0.003 μm^{-1} (Fig. 2C). We again found no obvious correlation. A linear fit to the mean values yields a slope of -0.025 and a correlation coefficient of only 0.17. These data provide no evidence for a positive correlation between the curvature and velocity, as required by Eq. 1.

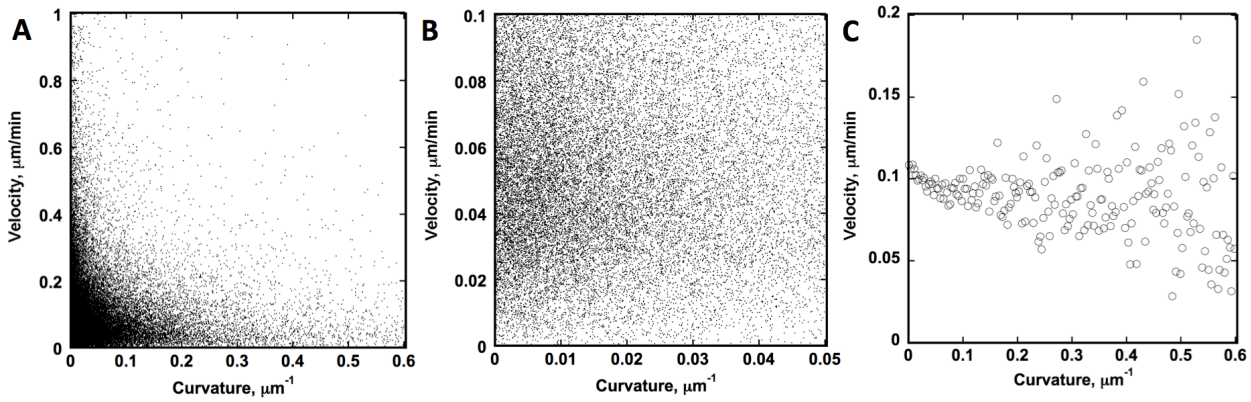

Fig. 2. The grain boundary velocity as a function of curvature. (**A**) Scatter plot showing the entire domain of the data. (**B**) A magnified view illustrating 84 % of the data. (**C**) Mean velocities of boundaries classified into curvature groups with widths of 0.003 μm^{-1}.

We also considered variations of the velocity with crystallographic parameters. We found the most substantial influence of the grain boundary crystallographic parameters on the velocity when we specify both the misorientation and the grain boundary plane orientation. For example, the mean velocities of [111] twist boundaries roughly doubles for boundaries with an approximately 40° twist angle (Fig. 3A). Similarly, the velocities of all symmetric tilt grain boundaries (STGBs) with rotations about the [100] axis and with $\Sigma \leq 49$, where Σ equals the inverse lattice coincidence (*27*), are relatively constant until tilt angles between 65° and 75°, where the boundary velocities are two to three times greater (Fig. 3B).

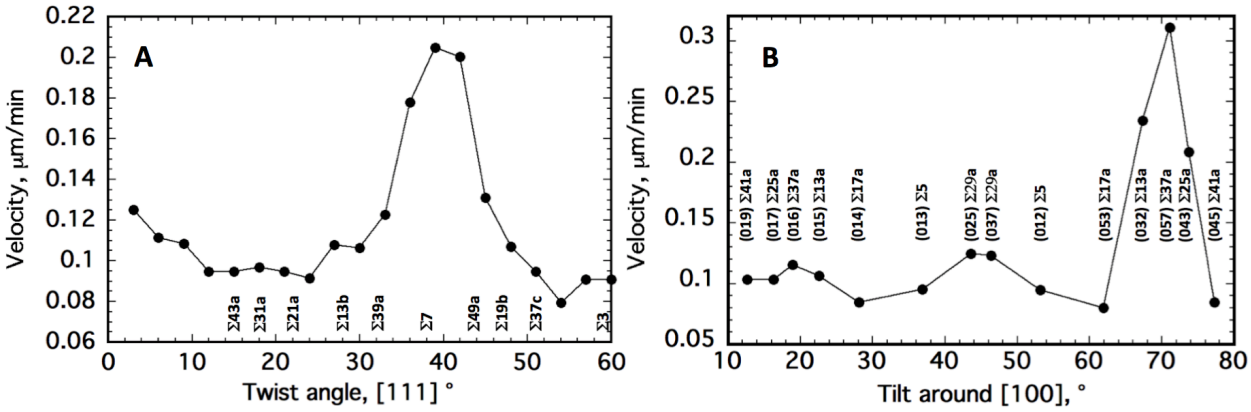

Fig. 3. Mean velocities as a function of crystallographic parameters (**A**) Twist grain boundaries for rotations about the [111] axis, in 3° intervals. These are boundaries whose planes are (111)$\|(\overline{111})$. For reference, the positions of coincident site lattice (CSL) (*27*) boundaries with $\Sigma \leq 49$ are indicated. (**B**) STGBs for all CSL boundaries with $\Sigma \leq 49$ and rotations about the [100] axis. The symmetric plane is listed for each boundary.

We can examine variations in the velocity with grain boundary plane orientation at fixed misorientation, as illustrated for the Σ3 misorientation (60° around [111]) (Fig. 4A). The coherent twin boundary at the (111) orientation has the minimum velocity, and tilt boundaries 90° from [111] have the maximum velocities. This observation is consistent with our expectations for Σ3 boundaries in fcc metals (*12, 28*). Our data also show that the coherent twin has the minimum curvature (Fig. 4B), consistent with the tendency of twin boundaries to be flat, as documented, for example, by curvature measurements of twins in an austenitic steel (*29*). The coherent twin is the most common boundary in Ni, which is reflected in its large relative area of 600 multiples of a random distribution (Fig. 4C). Finally, when our measured velocities are compared to previously computed grain boundary mobilities (*12*), we find the twin boundaries have both low mobility and low velocity, with the higher mobility boundaries 90° away. However, the $\{\overline{2}11\}$ type boundaries that have the maximum velocity (Fig. 4A) are predicted (Fig. 4D) to have low mobilities. Therefore, the velocities we observed are not well correlated with the computed mobilities, even if we divide the velocity by the curvature, which is relatively constant along the zone of tilt boundaries.

We also compared the velocity, curvature, population, and calculated mobility of the Σ7 boundaries (38.2° around [111]) (Fig. 4E-H), as they were among the highest velocity boundaries. The maximum velocities are in a broad peak near the orientation of the (111) twist grain boundary, where there is also a maximum in population (Fig. 4G) that can be attributed to a low grain boundary energy (*14*). All other orientations have smaller velocities. The curvature distribution (Fig. 4F) is nearly opposite to the velocity, with a local minimum in curvature at the twist position and maximum curvature along the positions of the tilt boundaries. The computed mobility distribution (Fig.

4H) contradicts the velocity distribution, and the differences cannot be explained by the observed curvature, which reinforces the differences. While the Σ3 boundary had the greatest area among all grain boundary types, the area of the Σ7 is more typical of all the other boundaries. We determined the Σ7 distribution from the evolution of 252 individual grain faces. Examples of some additional boundaries, consistent with the data for the Σ7 boundary, can be found in Figs. S6 and S7.

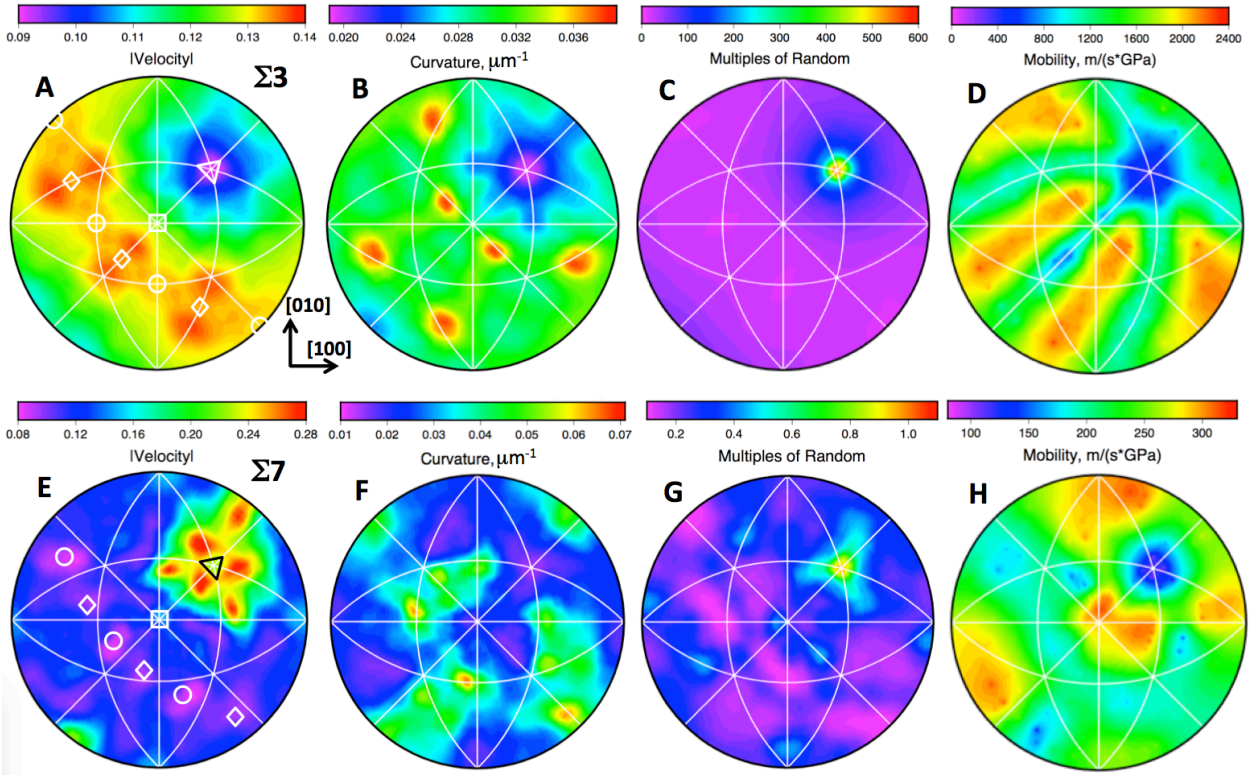

Fig. 4. Selected properties of Σ3 and Σ7 grain boundaries. The properties of Σ3 (**A**-**D**) and Σ7 (**E**-**H**) grain boundaries plotted on stereographic projections along [001]. The velocity (**A** & **E**) in μm/min, curvature (**B** & **F**), and relative areas (**C** & **G**) are from the current data. The grain boundary mobilities (**D** & **H**) are from Olmsted et al. (*12*) and were determined from molecular dynamics simulations at 1200 K and a driving force of 25 meV. In (**A**) and (**E**), the [001] direction is at the position of the white square, and the [111] misorientation axis is at the position of the triangle. In (**A**), the three white circles mark the orientations of the $\{\bar{1}10\}$ improper quasi-symmetric tilt boundaries, and the three white diamonds mark the orientations of the $\{\bar{2}11\}$ STGBs. In (**E**), the three white circles mark the orientations of the $\{\bar{3}21\}$ STGBs, and the three white diamonds mark the orientations of the $\{\bar{5}14\}$ improper quasi-symmetric tilt boundaries.

Finding literature data that can be used to make an exact comparison with our observed velocities of grain boundaries in a network is challenging. The closest existing data is that produced by MD simulations of Ni at 1200 K using an embedded atom potential (*12*). The calculations do not compare well to our observations (Figs. 4D,H). The largest difference between them is that the simulations are of bicrystals, so the boundary could move without the cooperative motion of attached boundaries. The high velocity we observed for boundaries in the vicinity of 40°

for [111] misorientations (Figs. 3A, 4E) is reminiscent of previous results for grain boundary migration in Al bicrystals (*30, 31*). However, in this previous work, the high velocity boundaries were cited to be of tilt character, while our high velocity boundaries have twist character.

Overall, we found little overlap between our observations of boundary migration in the polycrystal compared to experiments and simulations of bicrystals. This might not be too surprising considering the connectivity of the grain boundary network. While a boundary in a bicrystal clearly moves toward its center of curvature to reduce the interface free energy, a network of grain boundaries must evolve to lower the global energy of the network, which might not be compatible with all boundaries moving toward their centers of curvature. When a grain boundary migrates, it is also potentially changing the areas and orientations of all the boundaries to which it is connected. These boundaries will have different energies, and those energies are affected not only by the change in area, but also by changes in the grain boundary orientation (*14, 32*). The success of classical grain growth theories can be attributed to these details being averaged out, with the evolution of an ensemble of grains being subject only to the constraint of reducing the total grain boundary energy, rather than requiring each boundary to move towards its center of curvature. An example of this behavior is the formation and growth of corner twins in Ni which increases the total grain boundary area while simultaneously reducing the grain boundary energy (*21*). Similarly, it has also been shown that the migration of a boundary in recrystallizing Al is more dependent on the boundary plane inclination than the stored energy driving force (*33*).

One clear result from our observations is the dependence of the velocity on the five crystallographic grain boundary parameters. This finding suggests a strong dependence on grain boundary structure and would be a natural consequence of grain boundary migration mediated by disconnections (*34-36*). According to this theory, the rate of boundary migration remains proportional to curvature in a bicrystal but is mechanistically determined by the rate of disconnection nucleation and glide along the boundary. Each boundary has been shown to have a spectrum of disconnection nucleation energies (*36*). When the energy for disconnection nucleation is small and there are numerous modes that, acting together, can advance the boundary without accumulating large strains at the triple lines, boundaries are expected to have higher velocities than in cases where more energy for nucleation is required and there are fewer available modes. A detailed comparison between our results and disconnection mode spectra might lead to a better understanding of the relationship between grain boundary structure and velocity.

The influence of grain boundary crystallography on the observed velocities indicates that the driving force for grain boundary migration is more complex than depicted by Eq. 1. Because the grain boundary energies of Ni are

anisotropic (*14, 32*), the microstructure is expected to contain a mixture of flat singular boundaries (orientations at a deep cusp in the grain boundary energy) and smoothly curved non-singular boundaries. For singular boundaries, the driving force for migration is proportional to the weighted mean curvature, a quantity that depends more on the energies of the connected interfaces than on those of the moving interface (*37*). In this case, we do not expect a positive correlation between a grain boundary's velocity and its curvature, because Eq. 1 does not apply. Even for non-singular boundaries, differences between the grain boundary stiffness and the energy will degrade the predicted correlation between curvature and velocity (*15*).

Considering the fact that the boundary properties of Ni, Cu, Al, and Au are known to be highly correlated (*38*), our observations may well also apply to other technologically important metals with the fcc structure. The discovery that grain boundary velocities are not correlated to mean curvatures suggests that, for polycrystals, the traditional fundamental assumption about grain boundary migration is incorrect. Models based on this assumption are, therefore, potentially flawed. This might explain the failure of such models to predict microstructure-level details in the few cases in which grain-by-grain comparisons have been carried out between observations and simulations (*24, 39*). As an example of the limits of such models, curvature-driven grain growth simulations continue to evolve until all interfaces have been eliminated — a phenomenon that almost never occurs during real grain growth. More realistic models, which incorporate the influence of very slow moving grain boundaries (*18*) or the effects of shear-coupled motion (*40*), are able to reproduce the stagnation of grain size that occurs almost universally in isothermal growth experiments. Our findings suggest that a new model for grain boundary migration is needed to predict microstructure evolution. A necessary condition for the new model will be that it includes grain boundary crystallography, which is shown here to influence grain boundary migration kinetics. The disconnection-mediated grain boundary migration theory meets this condition (*36*).

References and Notes

1. K. Lu, L. Lu, S. Suresh, Strengthening Materials by Engineering Coherent Internal Boundaries at the Nanoscale. *Science* **324**, 349-352 (2009). doi: https://doi.org/10.1126/science.1159610.
2. L. Liu *et al.*, Making ultrastrong steel tough by grain-boundary delamination. *Science* **368**, 1347-1352 (2020). doi: https://doi.org/10.1126/science.aba9413.
3. C. A. Randall, N. Kim, J. P. Kucera, W. W. Cao, T. R. Shrout, Intrinsic and extrinsic size effects in fine-grained morphotropic-phase-boundary lead zirconate titanate ceramics. *J. Amer. Ceram. Soc.* **81**, 677-688 (1998). doi: https://doi.org/10.1111/j.1151-2916.1998.tb02389.x.
4. S. I. Kim *et al.*, Dense dislocation arrays embedded in grain boundaries for high-performance bulk thermoelectrics. *Science* **348**, 109-114 (2015). doi: https://doi.org/10.1126/science.aaa4166.

5. D. W. deQuilettes *et al.*, Impact of microstructure on local carrier lifetime in perovskite solar cells. *Science* **348**, 683-686 (2015). doi: https://doi.org/10.1126/science.aaa5333.
6. V. S. Solomatov, R. El-Khozondar, V. Tikare, Grain size in the lower mantle: constraints from numerical modeling of grain growth in two-phase systems. *Phys. Earth Planet. Inter.* **129**, 265-282 (2002). doi: https://doi.org/10.1016/s0031-9201(01)00295-3.
7. G. Durand *et al.*, Effect of impurities on grain growth in cold ice sheets. *J. Geophys. Res. Earth Surf.* **111**, (2006). doi: https://doi.org/10.1029/2005jf000320.
8. P. A. Beck, in *Metal Interfaces*. (American Society for Testing Materials, Cleveland, 1952), pp. 208-247.
9. G. Gottstein, D. A. Molodov, L. S. Shvindlerman, D. J. Srolovitz, M. Winning, Grain boundary migration: misorientation dependence. *Curr Opin Solid State Mater Sci* **5**, 9-14 (2001). doi: https://doi.org/10.1016/s1359-0286(00)00030-9.
10. M. Upmanyu, R. W. Smith, D. J. Srolovitz, Atomistic SImulation of Curvature Driven Grain Boundary Migration. *Inter. Sci.* **6**, 41-58 (1998). doi: https://doi.org/.
11. J. D. Powers, A. M. Glaeser, Grain boundary migration in ceramics. *Interface Science* **6**, 23-39 (1998). doi: https://doi.org/10.1023/a:1008656302007.
12. D. L. Olmsted, E. A. Holm, S. M. Foiles, Survey of computed grain boundary properties in face-centered cubic metals-II: Grain boundary mobility. *Acta Mater.* **57**, 3704-3713 (2009). doi: https://doi.org/10.1016/j.actamat.2009.04.015.
13. T. Frolov, Effect of interfacial structural phase transitions on the coupled motion of grain boundaries: A molecular dynamics study. *Applied Physics Letters* **104**, (2014). doi: https://doi.org/10.1063/1.4880715.
14. J. Li, S. J. Dillon, G. S. Rohrer, Relative grain boundary area and energy distributions in nickel. *Acta Mater.* **57**, 4304-4311 (2009). doi: https://doi.org/10.1016/j.actamat.2009.06.004.
15. F. Abdeljawad *et al.*, The role of the interface stiffness tensor on grain boundary dynamics. *Acta Mater.* **158**, 440-453 (2018). doi: https://doi.org/10.1016/j.actamat.2018.06.025.
16. C. Herring, in *Structure and Properties of Solid Surfaces; proceedings of a conference arranged by the National Research Council and held in September, 1952, in Lake Geneva, Wisconsin, USA.,* R. Gomer, C. S. Smith, Eds. (University of Chicago Press, Chicago, 1953), pp. 5-81.
17. W. M. Williams, C. S. Smith, A study of grain shape in an aluminum alloy and other applications of stereoscopic microradiography. *J. Metals* **4**, 755-765 (1952). doi: https://doi.org/.
18. E. A. Holm, S. M. Foiles, How Grain Growth Stops: A Mechanism for Grain-Growth Stagnation in Pure Materials. *Science* **328**, 1138-1141 (2010). doi: https://doi.org/10.1126/science.1187833.
19. J. Zhang *et al.*, Grain boundary mobilities in polycrystals. *Acta Materialia* **191**, 211-220 (2020). doi: https://doi.org/10.1016/j.actamat.2020.03.044.
20. J. V. Bernier, R. M. Suter, A. D. Rollett, J. D. Almer, High-Energy X-Ray Diffraction Microscopy in Materials Science. *Annu. Rev. Mater. Res.* **50**, 395-436 (2020). doi: https://doi.org/10.1146/annurev-matsci-070616124125.
21. B. Lin *et al.*, Observation of annealing twin nucleation at triple lines in nickel during grain growth. *Acta Mater.* **99**, 63-68 (2015). doi: https://doi.org/10.1016/j.actamat.2015.07.041.
22. J. M. Dake *et al.*, Direct observation of grain rotations during coarsening of a semisolid Al-Cu alloy. *Proc. Natl. Acad. Sci. U.S.A.* **113**, E5998-E6006 (2016). doi: https://doi.org/10.1073/pnas.1602293113.
23. A. Bhattacharya *et al.*, Three-dimensional observations of grain volume changes during annealing of polycrystalline Ni. *Acta Mater.* **167**, 40-50 (2019). doi: https://doi.org/10.1016/j.actamat.2019.01.022.
24. I. M. McKenna, S. O. Poulsen, E. M. Lauridsen, W. Ludwig, P. W. Voorhees, Grain growth in four dimensions: A comparison between simulation and experiment. *Acta Mater.* **78**, 125-134 (2014). doi: https://doi.org/10.1016/j.actamat.2014.06.028.
25. Y. F. Shen *et al.*, Importance of outliers: A three-dimensional study of coarsening in alpha-phase iron. *Phys. Rev. Mater.* **3**, (2019). doi: https://doi.org/10.1103/PhysRevMaterials.3.063611.
26. Materials and methods are available as supplementary materials.
27. B. L. Adams, J. Zhao, H. Grimmer, Discussion of the representation of intercrystalline misorientation in cubic materials. *Acta Cryst. A* **46**, 620-622 (1990). doi: https://doi.org/10.1107/s0108767390000435.
28. K. G. F. Janssens *et al.*, Computing the mobility of grain boundaries. *Nat. Mater.* **5**, 124-127 (2006). doi: https://doi.org/10.1038/nmat1559.
29. X. Zhong, D. J. Rowenhorst, H. Beladi, G. S. Rohrer, The five-parameter grain boundary curvature distribution in an austenitic and ferritic steel. *Acta Mater.* **123**, 136-145 (2017). doi: https://doi.org/10.1016/j.actamat.2016.10.030.

30. Y. Huang, F. J. Humphreys, Measurements of grain boundary mobility during recrystallization of a single-phase aluminium alloy. *Acta Mater.* **47**, 2259-2268 (1999). doi: https://doi.org/10.1016/s1359-6454(99)00062-2.
31. D. A. Molodov, U. Czubayko, G. Gottstein, L. S. Shvindlerman, Mobility of 111 tilt grain-boundaries in the vicinity of the special misorientation sigma=7 in bicrystals of pure aluminum. *Scripta Metall. Mater.* **32**, 529-534 (1995). doi: https://doi.org/10.1016/0956-716x(95)90832-5.
32. D. L. Olmsted, S. M. Foiles, E. A. Holm, Survey of computed grain boundary properties in face-centered cubic metals: I. Grain boundary energy. *Acta Mater.* **57**, 3694-3703 (2009). doi: https://doi.org/10.1016/j.actamat.2009.04.007.
33. C. Hong *et al.*, Recrystallization boundary migration in the 3D heterogeneous microstructure near a hardness indent. *Scripta Materialia* **205**, 114187 (2021). doi: https://doi.org/https://doi.org/10.1016/j.scriptamat.2021.114187.
34. K. Chen, J. Han, D. J. Srolovitz, On the temperature dependence of grain boundary mobility. *Acta Mater.* **194**, 412-421 (2020). doi: https://doi.org/10.1016/j.actamat.2020.04.057.
35. K. Chen, D. J. Srolovitz, J. Han, Grain-boundary topological phase transitions. *Proc. Natl. Acad. Sci. U.S.A.* **117**, 33077-33083 (2020). doi: https://doi.org/10.1073/pnas.2017390117.
36. J. Han, S. L. Thomas, D. J. Srolovitz, Grain-boundary kinetics: A unified approach. *Prog. Mater. Sci.* **98**, 386-476 (2018). doi: https://doi.org/10.1016/j.pmatsci.2018.05.004.
37. J. E. Taylor, Mean-curvature and weighted mean-curvature. 2. *Acta Metall. Mater.* **40**, 1475-1485 (1992). doi: https://doi.org/10.1016/0956-7151(92)90091-r.
38. E. A. Holm, D. L. Olmsted, S. M. Foiles, Comparing grain boundary energies in face-centered cubic metals: Al, Au, Cu and Ni. *Scripta Mater.* **63**, 905-908 (2010). doi: https://doi.org/10.1016/j.scriptamat.2010.06.040.
39. M. C. Demirel, A. P. Kuprat, D. C. George, A. D. Rollett, Bridging simulations and experiments in microstructure evolution. *Phys. Rev. Lett.* **90**, (2003). doi: https://doi.org/10.1103/PhysRevLett.90.016106.
40. E. Rabkin, D. J. Srolovitz, Grain growth stagnation in thin films due to shear-coupled grain boundary migration. *Scripta Mater.* **180**, 83-87 (2020). doi: https://doi.org/10.1016/j.scriptamat.2020.01.019.
41. C. M. Hefferan *et al.*, Statistics of High Purity Nickel Microstructure From High Energy X-ray Diffraction Microscopy. *CMC-Comput. Mat. Contin.* **14**, 209-219 (2009).
42. C. M. Hefferan, S. F. Li, J. Lind, R. M. Suter, Tests of microstructure reconstruction by forward modeling of high energy X-ray diffraction microscopy data. *Powder Diffraction* **25**, 132-137 (2010). doi: https://doi.org/10.1154/1.3427328.
43. M. A. Groeber, M. A. Jackson, DREAM.3D: A Digital Representation Environment for the Analysis of Microstructure in 3D. *Integrating Materials and Manufacturing Innovation* **3**, 5 (2014).
44. K. Glowinski, A. Morawiec, Analysis of Experimental Grain Boundary Distributions Based on Boundary-Space Metrics. *Metall. Mater. Trans. A* **45A**, 3189-3194 (2014). doi: https://doi.org/10.1007/s11661-014-2325-y.
45. http://mimp.materials.cmu.edu/~gr20/Grain_Boundary_Data_Archive/Ni_velocity/Ni_velocity.html

Acknowledgments:

Funding:

National Science Foundation under grant DMR 1628994 (GR, RS)

Advanced Photon Source, a U.S. Department of Energy (DOE) Office of Science User Facility operated for the DOE Office of Science by Argonne National Laboratory under Contract No. DE-AC02-06CH11357. (RS)

Author contributions:

Conceptualization: GSR, RMS, CEK

Methodology: AB, YFS, CMH, SFL, JL, RMS, CEK, GSR

Investigation: AB, YFS, CMH, SFL, JL

Visualization: AB, GSR

Funding acquisition: GSR, RMS

Project administration: GSR, RMS

Supervision: GSR, RMS

Writing – original draft: AB, GSR

Writing – review & editing: AB, RMS, CEK, GSR

Competing interests: Authors declare that they have no competing interests

Data and materials availability: The data and code used to for this paper will (upon publication) be made available at: http://mimp.materials.cmu.edu/~gr20/Grain_Boundary_Data_Archive

Supplementary Materials

Materials and Methods

Supplementary Text

Figs. S1 to S7

References (*41–44*)

https://science.org/doi/10.1126/science.abj3210

Supplementary Materials for

Grain boundary velocity and curvature are not correlated in Ni polycrystals

Aditi Bhattacharya, Yu-Feng Shen, Christopher M. Hefferan, Shiu Fai Li, Jonathan Lind, Robert M. Suter, Carl E. Krill III, Gregory S. Rohrer

Correspondence to: gr20@andrew.cmu.edu

This PDF file includes:

Materials and Methods

The preparation of the high-purity Ni sample discussed here, the acquisition of the HEDM data, and the assignment of orientations to each voxel have already been described in detail (*41,42*). Here we briefly recount some of the important details. Prior to the experiment, the high-purity Ni was annealed at 950 °C for 6 h (*41*), which led to a completely recrystallized microstructure. The X-ray data showed that the orientation spread within the grains was less than 0.1°. With a grain orientation spread of 0.1°, the geometrically necessary dislocation density is less than $2.5 \times 10^{11}/m^2$. The estimated driving force for boundary migration from dislocations (the product of the dislocation energy per length and the dislocation density) is therefore on the order of 1 kJ/m^3. On the other hand, the capillary driving force (grain boundary energy/mean radius) is on the order of 50 kJ/m^3. In other words, the capillary driving force is ≈ 50 times greater than the driving force associated with dislocations. After establishing the microstructure at 950 °C, orientation maps were obtained at six instances in time, separated by ≈ 30 min anneals at 800 °C. Here, we focus on the processing of the data and the extraction of the grain boundary velocities.

As described previously (*23*), the orientation maps were imported into DREAM.3D (*43*) for alignment and segmentation into grains. The result of this process was a set of three-dimensional orientation maps comprised of voxels that are 2.3 μm × 2.3 μm × 4 μm. The threshold defining a grain boundary was 2° of disorientation and the minimum grain size was 27 voxels. The microstructure contained about 2500 grains and the spherical equivalent average grain radius increased during the five annealing steps from about 19 μm to 23 μm microns or an ≈ 80 % volume increase. For the determination of grain boundary areas, grain boundary plane orientations, and grain boundary curvature, the boundaries were approximated by a triangular mesh and smoothed using DREAM.3D (*43*). Mean curvatures were also calculated in DREAM.3D, as described previously (*29)*.

For the present analysis, it is essential that the microstructures be in the same spatial reference frame so that a voxel-by-voxel comparison can be made between time steps. To achieve this, it was assumed that there is some rigid translation between successive states such that a voxel in the first volume corresponds to the same location as a voxel in the second volume and that at this translation, the average disorientation between voxels with the same index in the two volumes will be a minimum. To find this translation, the average disorientation ($\overline{\Delta g}$) between the voxels in the two volumes in neighboring times steps (t = 1,2) was computed as:

$$\overline{\Delta g} = \frac{\sum_{k=1}^{Z}\sum_{j=1}^{Y}\sum_{i=1}^{X} g_{ijk|t=1} g_{ijk|t=2}^{T}}{N}, \qquad \text{(S1)}$$

where X, Y, and Z are the numbers of voxels in the three perpendicular directions, g is a three-by-three matrix representing the voxel orientation, and N is the number of locations where the position i, j, k at both t = 1 and t = 2 contains non-zero data. Beginning from an approximate alignment, the average disorientation is computed for the smallest 729 translations produced by the vectors $u\vec{x} + v\vec{y} + w\vec{z}$, with $\vec{x}$, $\vec{y}$, and $\vec{z}$ being elementary voxel-to-neighbor voxel translations and u, v, and w taking all integer values between -4 and +4. In all the cases examined, the minimum disorientation was a unique and global minimum for all possible translations. To complete the alignment, the second volume is translated to the position of minimum average disorientation.

Figure S1 schematically defines all of the quantities in Eq. 2. When the velocity is computed using Eq. 2 of the main text, an absolute value is applied because the value is unsigned. Grain boundaries have crystal exchange symmetry—in the sense that the five parameters needed to specify the macroscopic degrees of freedom of a given boundary location remain unchanged if the grain labels n and m are exchanged. So from the point of view of the boundary, there is no sign associated with v. In principle, the two volume terms in the numerator on the right-hand side of Eq. 2 could be added or subtracted from each other. The minus choice provides a net volume exchange and the plus is a total volume change. Note that the boundary can move in such a way that equal volumes transfer from n to m and m to n, resulting in a zero net velocity (using the minus sign). However, volume was exchanged, and this required some motion of the boundary, which will be reflected in the total volume change (using the plus sign). We computed velocities by both methods and compared them. Naturally, the velocities computed with the plus sign had larger magnitudes; however, the shapes of the distributions were the same for each choice. The results presented here are for the total volume change (plus choice). Table S1 provides the numerical data for the two grains in Fig. 1 that were used to calculate the grain boundary velocity.

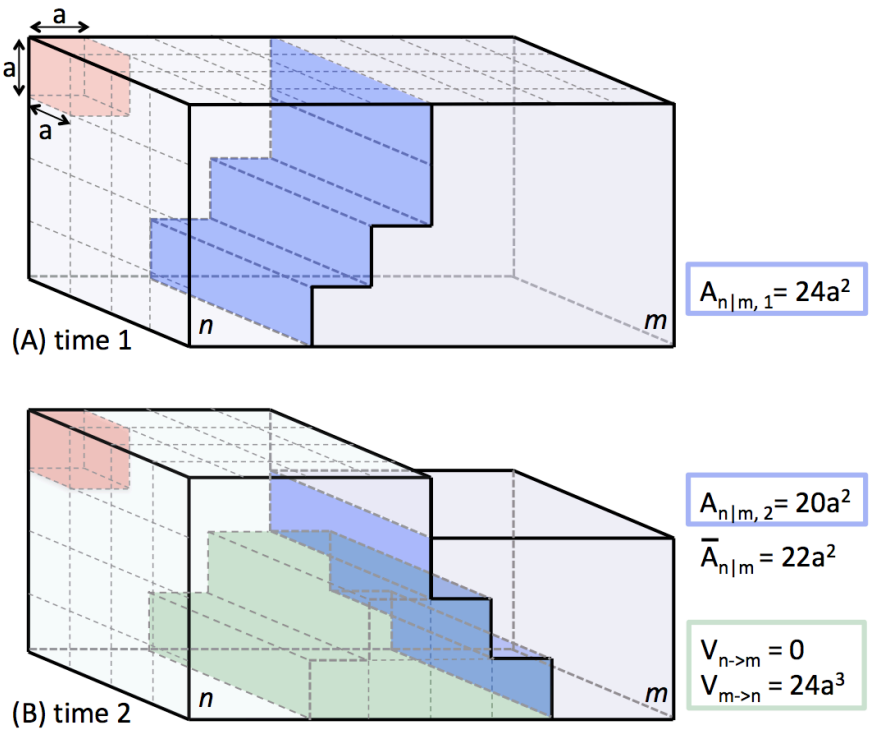

Fig. S1. Schematic illustration of the calculation of grain boundary velocities.
The schematic shows two grains, *n* and *m*, separated by a boundary (shaded blue). (A) The thin grey dashed lines on the left side and top of the parallelepiped mark the boundaries of individual voxels. One complete a × a × a voxel is shaded red and shown in the upper, left rear corner. For simplicity, we use cubic voxels here in contrast to the tetragonal shape illustrated in Fig. 1A which was used in the analysis of the experimental data. The total area of the stepped boundary is $24a^2$. (B) After an annealing interval (time 2 – time 1), 24 of the voxels originally in grain *m* are now part of grain *n* (shaded green). No voxels have moved from *n* to *m*. The boundary between *n* and *m* (shaded blue) has migrated to a new location and its area has also decreased to $20a^2$. The quantity $\bar{A}_{n|m}$ is calculated as the average of the boundary area at time 1 and time 2.

Table S1. Data employed in calculating the velocity of the boundary in Figure 1

time step	$A_{n\|m}$ (μm^2)	$\bar{A}_{n\|m}$ (μm^2)	$V_{n->m}$ (voxels)	$V_{m->n}$ (voxels)	Δt (min)	v (μm/min)
0	3.44×10^3	-	-	-	-	
1	3.64×10^3	3.54×10^3	0	530	23	1.38×10^{-1}
2	2.31×10^3	2.89×10^3	0	269	30	6.57×10^{-2}

The velocities for each face were applied to each triangular mesh element so that at each element of the mesh, we know the local orientation (normal to the triangle), area, grain face curvature, and grain face velocity. A separate analysis where each triangle was assigned the local curvature led to similar results and supported the same conclusions. We note that the approach we use here, of assigning a single velocity to all of the orientations of a curved grain boundary, is comparable to prior experimental (9) and simulation (10) studies of curved bicrystals.

The analysis resulted in velocities for 53,775 grain boundaries (the boundary between *n* and *m* in Fig. 1A,B is an example of one of these boundaries). The distribution of face velocities is illustrated in Fig. S2A. When the velocity distributions for each time step were considered separately, there were no systematic differences. Therefore, the data from all of the time steps are combined and considered together. The mean velocity is 0.1 μm/min and the standard deviation is approximately the same order. The tail of this distribution extends to 60 μm/min; these very large values are assumed to be non-physical, resulting from artifacts in reconstruction of the microstructure of the two states. Therefore, the distribution was cut off at 1 μm/min (which is more than eight standard deviations from the mean). This condition eliminated 345 faces. The distribution of face curvatures is illustrated in fig. S2B. The face curvature is the average curvature of all triangular mesh elements on a boundary between two grains. The mean curvature is 0.05 μm^{-1} and the standard deviation is 0.08 μm^{-1}. Note that the magnitude of the mean corresponds to grains with a mean radius of 20 μm, consistent with the average grain size in

this microstructure. The curvature calculation yields large non-physical values near the triple lines, where the data are not smoothed. The spherical equivalent radius of a single voxel is the smallest measured feature and this can be used to determine the maximum observable curvature, which is 0.6 μm^{-1}. Therefore, faces with curvatures greater than 0.6 μm^{-1} (1636 faces) were eliminated. After filtering according to these conditions, 51794 faces remained for analysis, each with a computed velocity and curvature. These values were assigned to the appropriate triangles in the grain boundary mesh, which was made up of approximately 1.8×10^7 triangles.

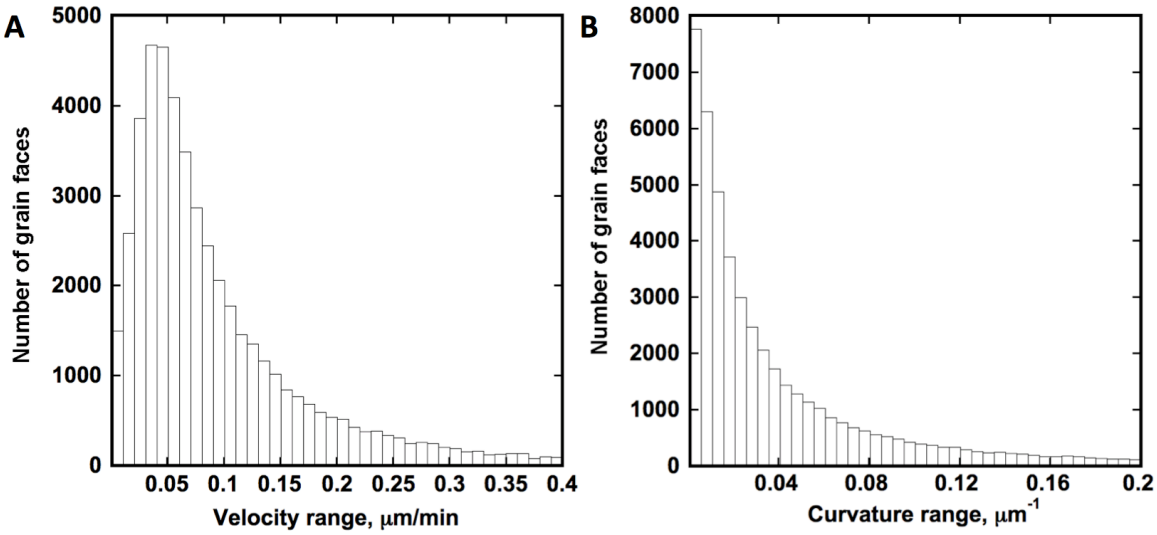

Fig. S2. Grain velocity and curvature distributions

(**A**) Histogram of measured grain boundary velocities. (**B**) Histogram of average grain boundary curvatures for each face. Both distributions are truncated to emphasize the most highly populated categories.

If the triple lines had a measurable influence on the boundary motion, we would hypothesize that small faces ought to be more affected than larger faces. To determine whether or not a correlation between mean curvature and velocity might exist for the largest or smallest faces, they were divided into two groups: the larger faces (areas greater than 1000 μm^2) and the smaller faces (areas less than 1000 μm^2). As illustrated in Fig. S3, neither group manifests a noticeable degree of correlation. To test whether or not the sizes of the curvature groups in Fig. 2C influence the result, we have also discretized the data into fewer bins twice as wide (Fig. S4A) or more bins half as wide (Fig. S4B). Changing the bin size does not lead to a qualitatively different result. Finally, we also analyzed the unfiltered data (Fig. S5A) and the data after more aggressive filtering, which removed all velocities and curvatures more than three standard deviations from the mean (Fig. S5B). In both cases, the results were similar to Fig. 1C and supported the same conclusions.

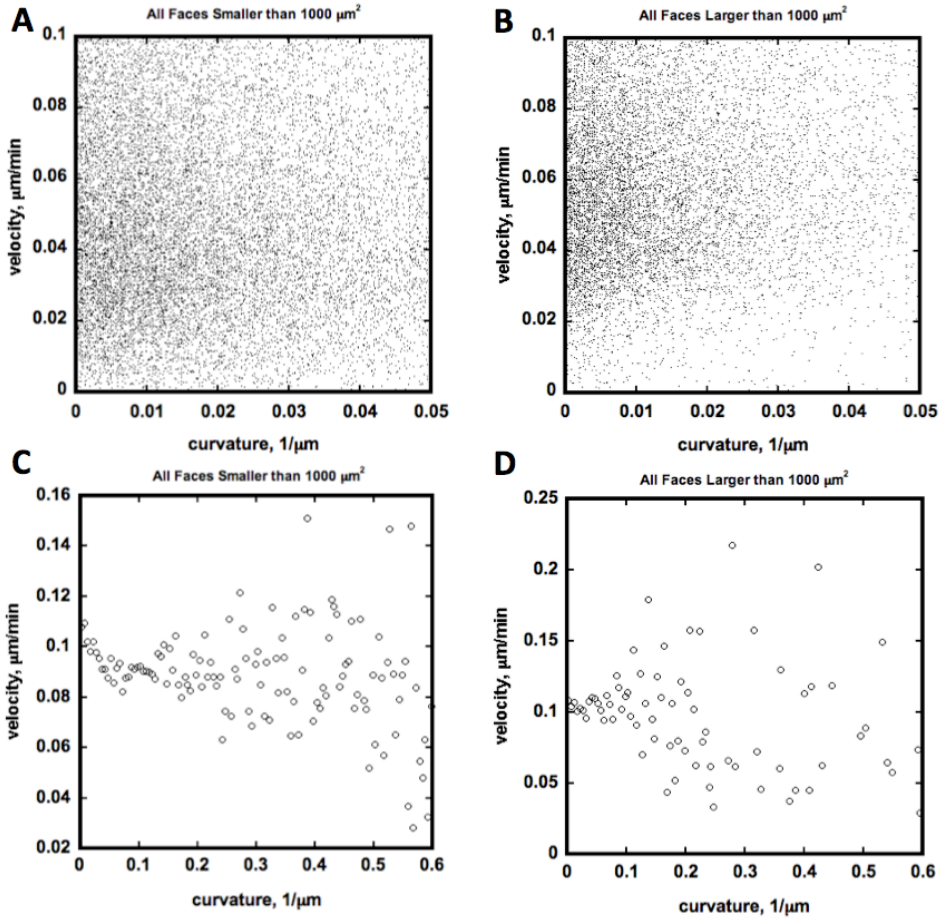

Fig. S3. The grain boundary velocity as a function of curvature.
Scatter plots for (A) smaller and (B) larger grain faces. The domain of these plots has been reduced to show the trends in the majority (84 %) of the data, as in Fig. 1B. Mean values of the data in (A) and shown in (C) and mean values of the data in (B) and shown in (D).

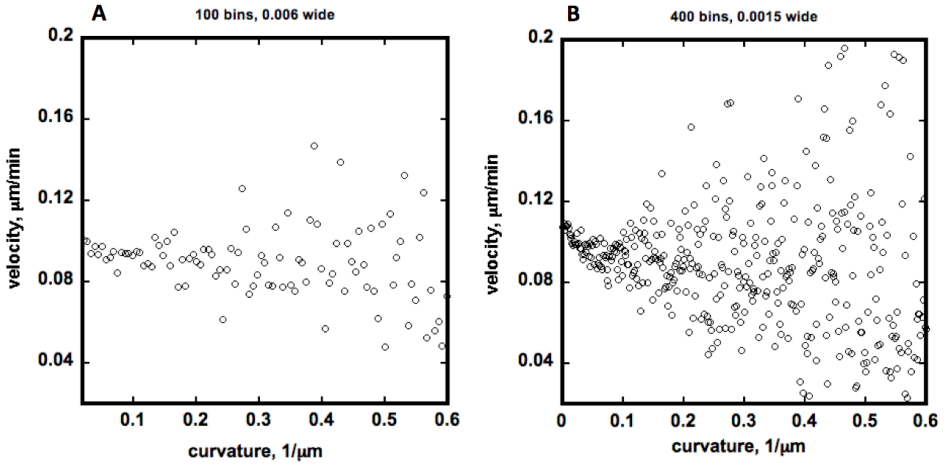

Figure S4. Mean velocities using different discretization schemes.
Mean velocities of boundaries classified into curvature groups, for comparison to Fig. 2C. A) Curvature groups with widths of 0.006 μm^{-1}. B) Curvature groups with widths of 0.0015 μm^{-1}.

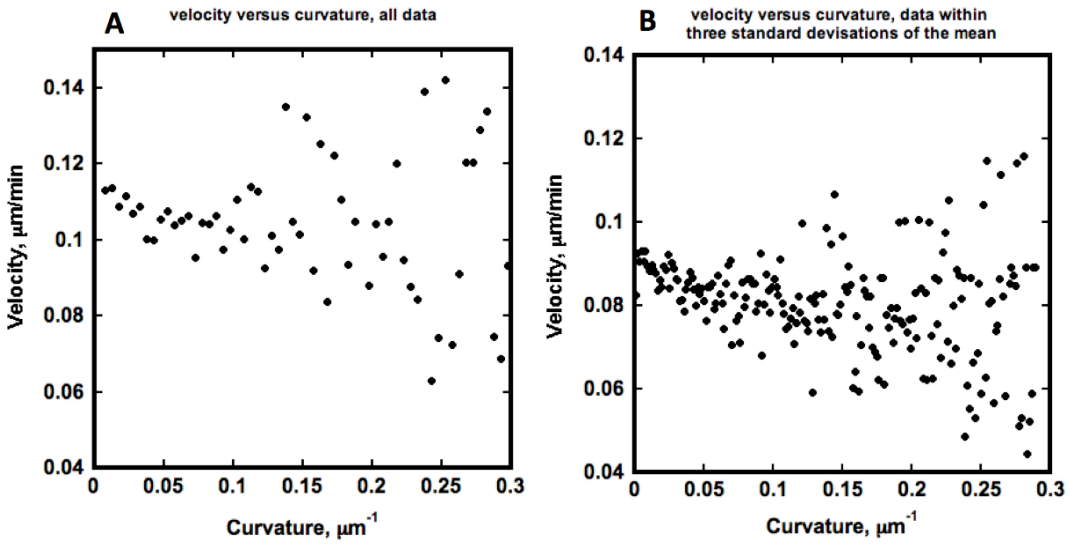

Fig. S5. Mean velocities using different thresholds for outliers.
Mean velocities of boundaries classified into curvature groups, for comparison to Fig. 2C. A) This plot includes all data. Curvature values are grouped into bins of width 0.01 μm^{-1}. B) Data within three standard deviations of the mean. Here, the curvature values are grouped into bins of width 0.0015 μm^{-1}.

The determination of grain boundary properties as a function of crystallographic parameters was carried out using the method of Glowinski and Morawiec (*44*). Given five coordinates that specify the boundary crystallography, all triangular mesh elements that fall within a fixed aperture (5° wide in misorientation space and 7° wide in grain boundary plane orientation space) are identified and averaged. The calculated mobility data were taken from the supplemental information provided by Olmsted et al. (*12*).

Supplementary Text

To complement Fig. 4 in the main part of the manuscript, comparable data for the Σ5 (36.9° around [100]) and Σ9 (39.9° around [110]) grain boundaries are plotted in Fig. S6. Velocity and curvature data for the Σ37a and Σ27a are shown in Fig. S7 because these misorientations have the greatest velocities for all symmetric tilt grain boundaries (STGBs) with $\Sigma \leq 49$ around the [100] and [110] axes, respectively. For the Σ37a boundary (18.9° around [100]), the maximum velocity is within measurement resolution of the orientation of the {057} STGB (Fig. S7A). This orientation is a local minimum in the curvature. Note that the other STGB at this misorientation, {016}, has a much lower velocity. The curvature distribution, on the other hand, has a maximum at a mixed boundary (Fig. S7B), emphasizing the lack of correlation between curvature and velocity. The velocity and curvature distributions at the Σ27a (31.6° around [110]) boundary are illustrated in Fig. S7 C and D. In this case, there is a local maximum in the velocity at the {115} STGB orientation and another broad local maximum at the $(1\bar{4}6)||(14\bar{6})$ twist boundary. A comparison of the velocity and curvature distributions for the Σ27a boundaries supports the absence of a positive correlation between the two quantities.

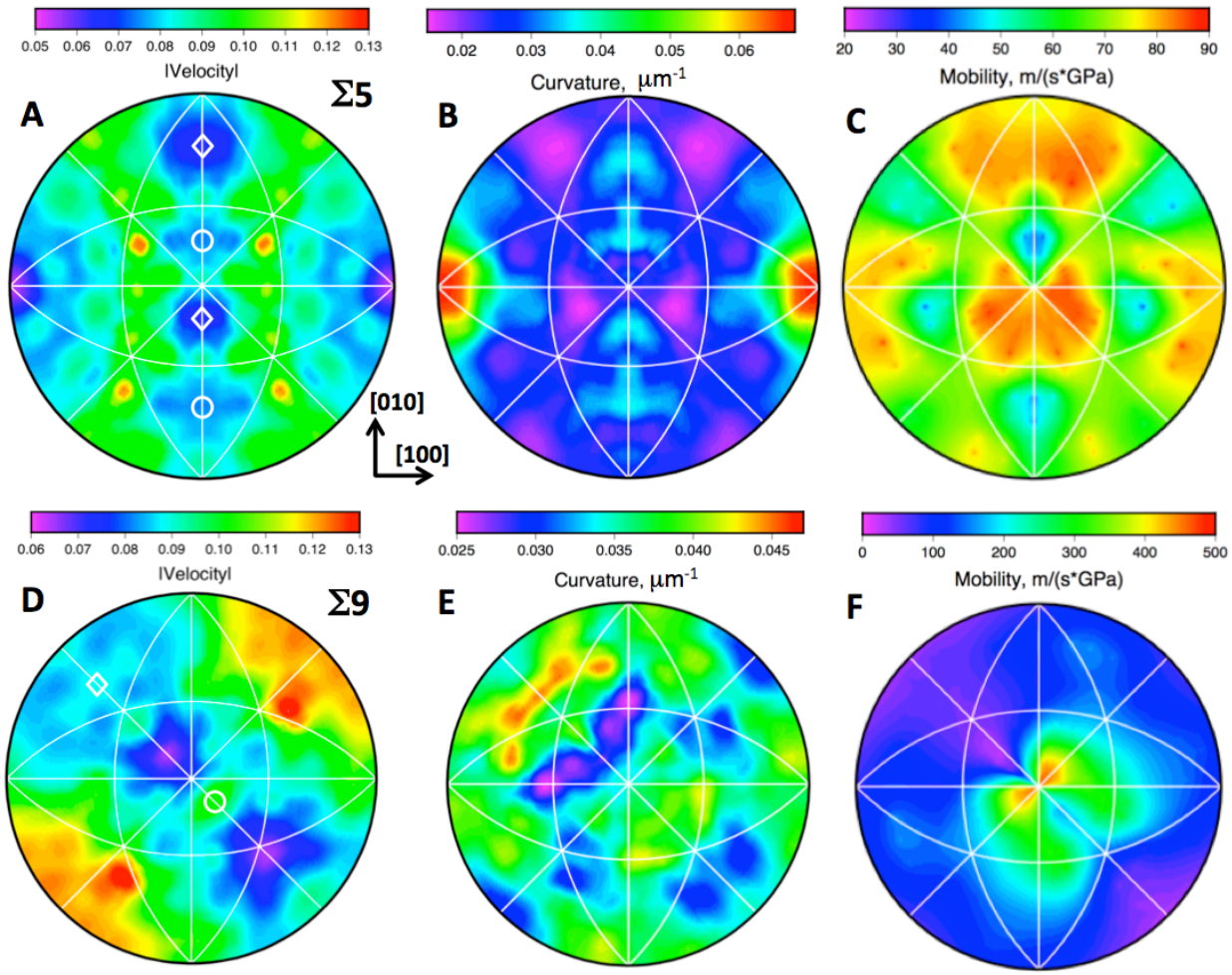

Fig. S6. The properties of Σ5 and Σ9 boundaries

The properties of Σ5 (**A**-**C**) and Σ9 (**D**-**F**) grain boundaries plotted on stereographic projections along [001], in the same reference frame as Fig. 4. The velocity, in μm/min, (**A** & **D**), curvature (**B** & **E**), and mobilities (**C** & **F**). The mobility values are from Olmsted et al. (*24*) and determined from molecular dynamics simulations at 1200 K and a driving force of 25 meV. In (**A**), the white circles mark the {013} STGB orientations and the white diamonds mark the {012} STGB orientations. In (**D**), the white circle marks the {114} STGB and the white diamond marks the {221} STGB.

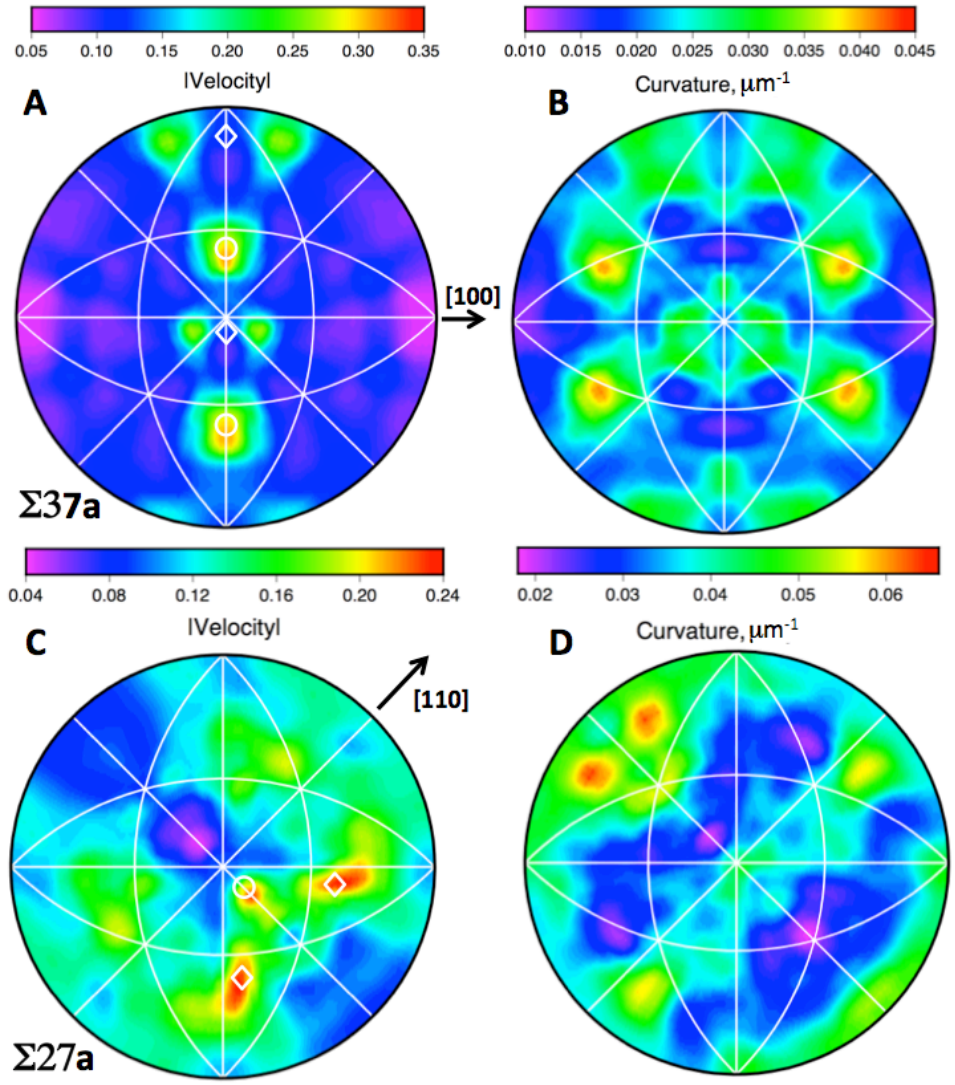

Fig. S7. Properties of Σ37a and Σ27a boundaries

The properties of Σ37a (**A**-**B**) and Σ27a (c-d) grain boundaries plotted on stereographic projections along [001], in the same reference frame as Fig. 4 of the main text. The velocity, in μm/min, (**A** & **C**), and curvature (**B** & **D**) of the boundaries are shown. The misorientation axis, which is in the plane of the paper, is shown for each boundary. In (**A**), the white circles mark the positions of the {057} STGBs and the white diamonds mark the positions of the {016} STGBs. In (**C**), the white circle marks the position of the {115} STGB and the white diamonds mark the positions of the $(1\bar{4}6)||(14\bar{6})$ twist boundaries.